

Design of a Sensor Based on CSRR-Derived Structures for Characterizing Permittivity and Permeability Simultaneously

Hong-Gang Hao¹, Yun-Rui Wang^{1,3,*}, Bing Wang¹, Ye Zhang¹, and Xing-Rui Ni²

¹College of Optoelectronic Engineering, Chongqing University of Posts and Telecommunications, Chongqing 400065, China

²Chongqing Liangjiang Satellite Mobile Communication Co., Ltd., Chongqing 401121, China

³China Telecom Corporation Chengdu Branch, Chengdu 610066, China

ABSTRACT: A dualport microstrip sensor based on a complementary split ring resonator (CSRR)-derived structure is proposed to measure the permittivity and permeability simultaneously in this paper. The coupling among meandered conductive ring, interdigital capacitor, and microstrip line is used to obtain the relatively independent distribution area of the highest intensity of the electric field and magnetic field. It can be utilized to distinguish the influence of permittivity and permeability on the resonant frequency point. A numerical model was established for extracting the magnetic and dielectric properties, and the sensor was processed and tested. The findings demonstrate that the sensor can measure permittivity and permeability in a single operation by taking advantage of the resonant properties of low and high frequencies. The relative errors of the measured permittivity and permeability are controlled within 4.43% and 3.41%, as well as the sensitivity values S_{fm} and S_{fe} of 7.24 and 3.06, indicating excellent overall performance.

1. INTRODUCTION

The accurate detection of material permeability and permittivity is crucial in a variety of disciplines, including biomedical [1], manufacturing, industrial [2], and military [3] fields. Different methods can be used according to the application environment and the type of sample under test (SUT), such as transmission line method [4], free space method [5], waveguide method [6], and near-field method [7]. Within the microwave frequency range, methods for characterizing materials can be simply classified into resonant method and non-resonant method. Resonant method uses resonant frequency and quality factor changes caused by the resonator after loading the SUT to obtain material properties. It can effectively assess material properties at single or discrete frequencies and has a higher sensitivity and precision than the non-resonant technique [8].

In recent years, planar microwave resonant sensors based on split ring resonator (SRR) and complementary split ring resonator (CSRR) structures have been applied to the detection of various materials due to their high sensitivity, compact size, and low cost [9]. For example, a microstrip sensor loaded with two SRRs is designed to characterize solid dielectric samples in [10], and its differential design can improve the robustness to environmental factors. In [11], two improved structures based on CSRR resonators are proposed, which can be used to the measure permeability. It is shown that new resonator designs reduce the error due to permittivity variations by 79%. In addition, a sensor for characterizing the full properties of magneto-dielectric materials based on CSRR is introduced in [12]. The sensor locates the maximum intensity of the electric field and the magnetic field in two different regions to obtain the permittivity and permeability of the SUT, respectively. Reference

[13] developed a CSRR loaded on a microstrip line to comprehensively characterize magneto-dielectric materials in a single run of measurement. The real parts of its complex permittivity and complex permeability can be extracted from the resonant frequency.

It is not difficult to see that there might be some improvements over the previous design. For example, some sensors measure only one type of parameter, either permittivity or permeability. For sensors that can fully detect the two types of parameters, most of them need to run several times to complete the material testing of samples. Although the latest research shows that the permittivity and permeability can be retrieved in one operation, only their real parts are taken into account, while the imaginary parts (electric loss tangent and magnetic loss tangent) are omitted. Therefore, a sensor is introduced in this study that can characterize the real and imaginary parts of the permittivity and permeability of the SUT in a single run, enabling the sensor to achieve straightforward measurement and obtain more accurate electromagnetic information. The CSRR-derived structure loaded with microstrip lines is the basis of the sensor construction. The etched meandered conductive ring and interdigital capacitor in the CSRR-derived structure can separate the permittivity sensing area from the permeability sensing area. Moreover, they can greatly enhance the intensity of the electric and magnetic fields, making the sensor more sensitive and less expensive.

2. SENSOR WORKING PRINCIPLE AND STRUCTURE

2.1. Working Principle

According to the principle of detecting electromagnetic parameters by resonant method and perturbation theory, the original distribution of the electric and magnetic fields is perturbed

* Corresponding author: Yun-Rui Wang (645820206@qq.com).

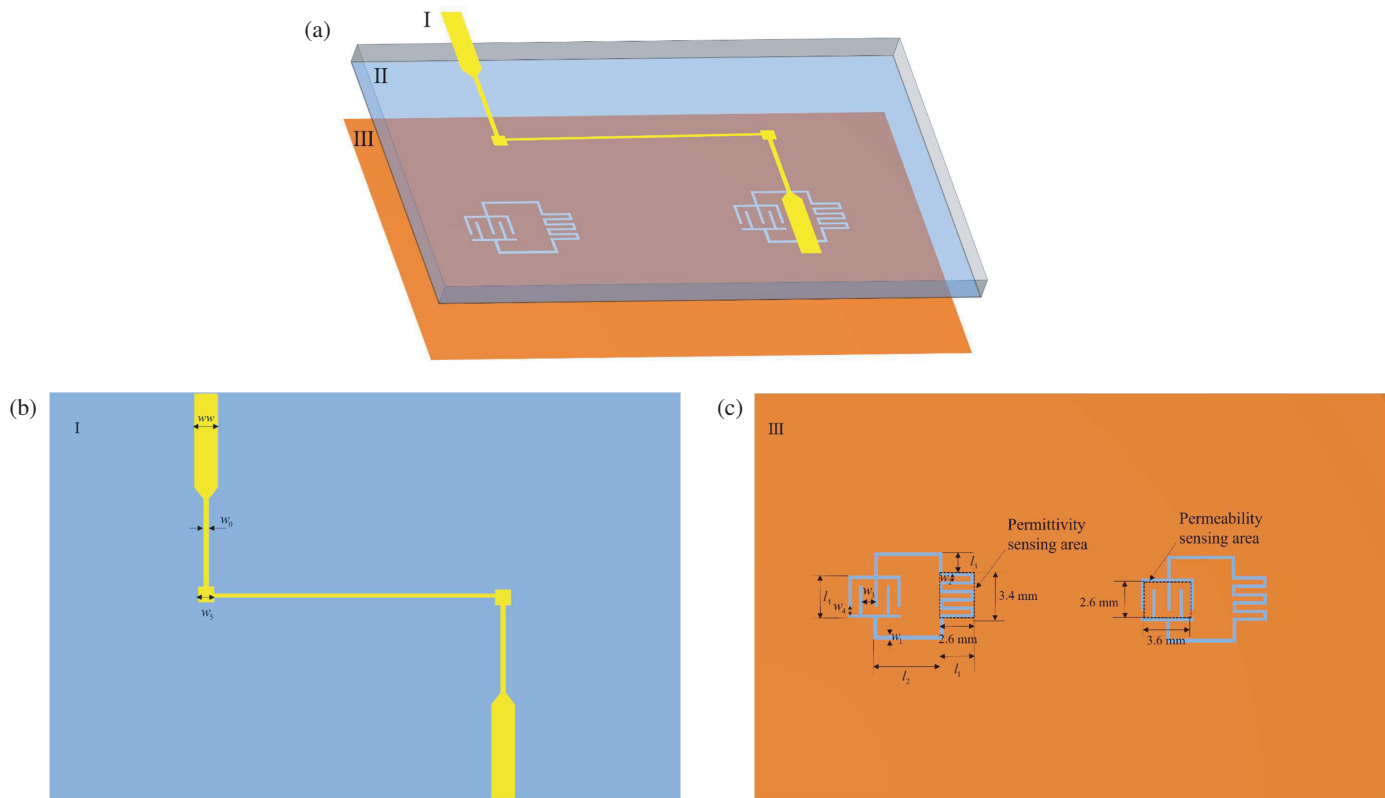


FIGURE 1. Geometry of the proposed sensor, (a) exploded view, (b) top view, (c) bottom view.

when the sample is placed on the microwave structure sensor. As a result, the resonator's frequency and quality factor will change [14]. The relation between the sensor's response and the material properties can be expressed as

$$\frac{\Delta f_r}{f_r} = \frac{\int_v (\Delta \varepsilon \mathbf{E}_1 \cdot \mathbf{E}_0 + \Delta \mu \mathbf{H}_1 \cdot \mathbf{H}_0) dv}{\int_v (\varepsilon_0 |\mathbf{E}_0|^2 + \mu_0 |\mathbf{H}_0|^2) dv} \quad (1)$$

where Δf_r is the change of resonant frequency after placing the sample; f_r is the initial resonant frequency, and v is the perturbation volume; ε_0 and μ_0 represent the permittivity and permeability in vacuum. \mathbf{E}_0 and \mathbf{H}_0 are the field distributions without loading of the SUT; \mathbf{E}_1 and \mathbf{H}_1 are the electric and magnetic field distributions in the presence of the sample; $\Delta \varepsilon$ and $\Delta \mu$ are the changes in permittivity and permeability. For extremely low power resonators with minimal variation in the magnitude of the fields before and after the resonance, the relation can be simplified as follows [15].

$$\frac{\Delta f_r}{f_r} = \frac{\int_v (\Delta \varepsilon |\mathbf{E}_0|^2 + \Delta \mu |\mathbf{H}_0|^2) dv}{\int_v (\varepsilon_0 |\mathbf{E}_0|^2 + \mu_0 |\mathbf{H}_0|^2) dv} \quad (2)$$

From (2), if the magnetic field has a high strength, and the electric field has a very low strength, the change of the permittivity has no significant effect on the resonant properties, but the permeability can markedly change the resonant properties. Similarly, if the electric field is localized with high intensity, but the magnetic field is very weak, the resonant properties can

be obviously influenced by permittivity of the sample, independent of the permeability. The above analysis implies that the change of sensor resonant characteristics is correlated with the permittivity and permeability of SUT, but the premise is that the area with relatively independent electric and magnetic field distributions can be obtained in the structural design of the microwave sensor. If the sensor has only one resonant frequency point in one measurement, it may be a challenge to identify whether the resonant characteristic is related to permeability or permittivity. In order to detect the permittivity and permeability simultaneously, a microwave sensor with two resonant frequencies is designed in this study, which makes different resonant frequencies closely associated with different material properties.

2.2. Sensor Structure

The geometrical structure of the sensor is depicted in Fig. 1. On the top, a dual port microstrip line with a 2.35 mm width is used to provide a 50 Ω characteristic impedance. The substrate is Rogers 5880, which has a thickness of 0.787 mm, a loss tangent of 0.0009, and a dielectric constant of 2.2. Two CSRR-derived structures are etched at the bottom on a metal ground plate with a 0.035 mm thickness. A concentrated electric and magnetic field can be produced by the structure, which is made up of a meandered conductive ring and an interdigital capacitor. To prevent mutual coupling, the distance between the two CSRR-derived structures must also be sufficient. Two CSRRs are also used as sensing units to measure the permittiv-

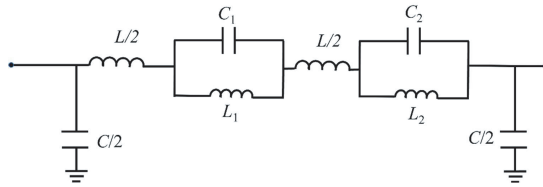


FIGURE 2. Equivalent circuit model for proposed sensor.

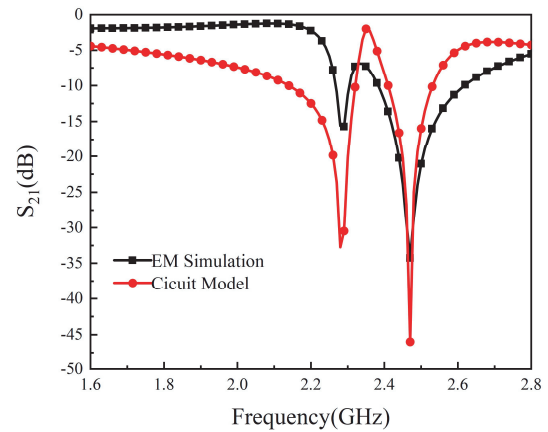


FIGURE 3. Comparison between the circuit model results and the EM simulation results of the proposed sensor when unloaded.

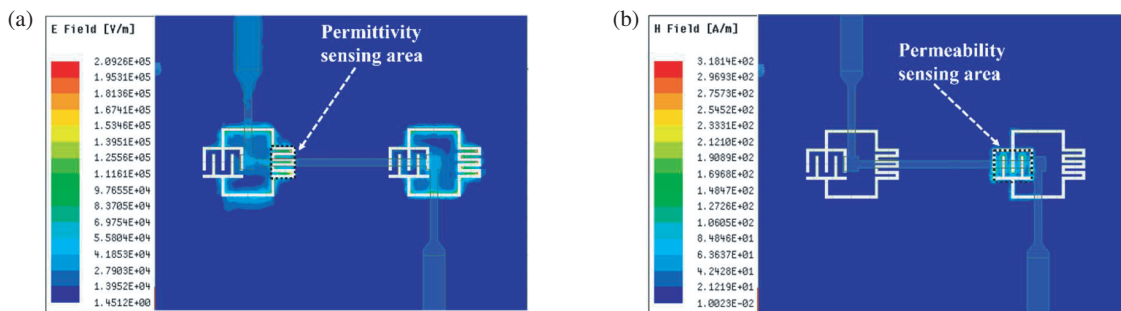


FIGURE 4. Magnitude distributions of (a) electric field and (b) magnetic field on the ground plane at the resonant frequency.

ity and permeability. The precise geometric parameters of the optimized sensor are shown in Table 1. The sensor is oriented from [16], but compared to [16], the performance of the sensor has been greatly improved by the use of a meandered conductive ring and an interdigital capacitor. These components significantly enhance the electric field strength and magnetic field strength of the permittivity sensing area and the permeability sensing area at the resonant frequency and increase the interaction between the field and the SUT.

TABLE 1. Geometrical parameters of the proposed sensor.

Parameter	Value (mm)	Parameter	Value (mm)
l_1	2.6	w_1	0.4
l_2	5.4	w_2	0.2
l_3	2.0	w_3	0.6
l_4	3.4	w_4	0.4
ww	2.35	w_5	1.6
w_0	0.8		

Regardless of the losses in the design, the equivalent circuit model of the sensor is shown in Fig. 2 [17]. The CSRR structures are magnetically coupled with the microstrip line. Each CSRR unit is represented by the combination of inductor L_i and capacitor C_i , where $i = 1, 2$. The microstrip line is modeled

with inductor L , and C is the coupling capacitor between the microstrip line and the etching ring. Because the two CSRRs are located at different positions of the microstrip line, their parameters are asymmetric, that is, $C_1 \neq C_2$, $L_1 \neq L_2$, so that the two transmission zeros (f_{r1} , f_{r2}) will always exist in the circuit.

The values of the lumped element in equivalent circuit are extracted using the Advanced Design System (ADS), $C_1 = 2.3$ pF, $L_1 = 2.11$ nH, $C_2 = 1.96$ pF, $L_2 = 2.12$ nH, $C = 0.58$ pF, $L = 8.4$ nH. Fig. 3 shows the results of electromagnetic structure simulation using high-frequency structure simulator (HFSS) and circuit simulation using ADS. Their consistent transmission response proves the feasibility of the equivalent circuit.

$$f_{r1} = \frac{1}{2\pi\sqrt{L_1 C_1}} \quad (3)$$

$$f_{r2} = \frac{1}{2\pi\sqrt{L_2 C_2}} \quad (4)$$

Figures 4(a) and (b) show the electric and magnetic field distributions on the metal ground plane of the sensor at the resonance. It can be observed from Fig. 4 that the magnetic field strength is almost zero, and the electric field strength is very high in the etched meandered conductive ring. This area can be used as the permittivity sensing area to characterize the dielectric properties of the material. On the contrary, there is an

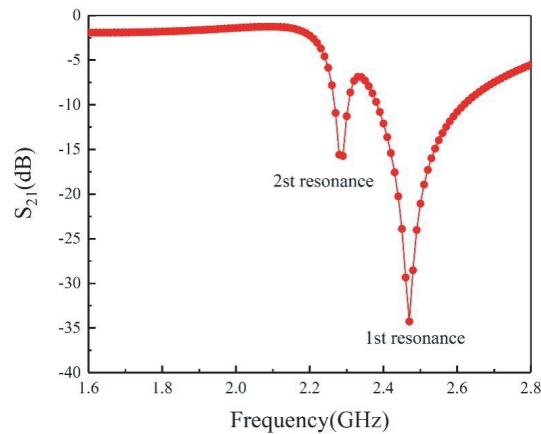


FIGURE 5. Frequency response of the proposed sensor when unloaded.

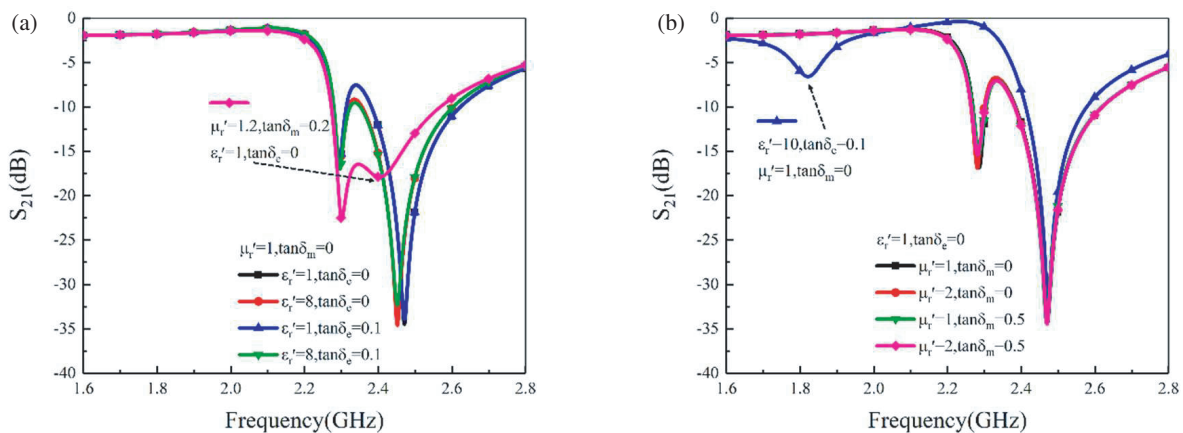


FIGURE 6. The sensor response of the sample loaded on (a) the permeability sensing area and (b) permittivity sensing area.

extremely strong magnetic field and a weak electric field in the etched interdigital capacitor, which can be used as the permeability sensing area to characterize the magnetic properties of materials.

3. RESULTS AND ANALYSIS

In practice, the variation ranges of ϵ_r' and $\tan \delta_e$ of magneto-dielectric materials in microwave are $1 \sim 10$ and $0 \sim 0.1$, and μ_r' and $\tan \delta_m$ vary from $1 \sim 2$ and $0 \sim 0.5$, respectively [18]. There is no doubt that the presence of air will have a certain impact on the measurement process, so it is taken into account that there is $15 \mu\text{m}$ air gap between the SUT and metal ground to ensure the objectivity in the simulation. It should also be noted that the thickness of the SUT will affect the response of the sensor. With the increase of sample thickness, the interaction between the field and the sample is enhanced, and the change in sensor response will also increase. However, the field distribution in the sensing area is highly concentrated, and the response of the sensor will basically remain unchanged when the SUT thickness exceeds 0.5 mm . Therefore, the sample thickness is set to 0.5 mm in this paper.

The frequency response of the sensor when it is unloaded is shown in Fig. 5. It can be seen that there are two resonant points

used to characterize the dielectric parameters and magnetic parameters of the magneto-dielectric material, and their resonant frequencies are 2.473 GHz and 2.286 GHz , respectively.

For the convenience of numerical model analysis and discussion, the normalized resonant frequency shift is defined as f_{ni} , $f_{ni} = (f_{ui} - f_{ri})/f_{ui}$, where f_{ui} and f_{ri} are the frequencies of the i th resonant point under unloaded and after the sample is loaded. The quality factor $Q = f_r/\Delta f$, f_r is the resonant frequency, and Δf is the 3-dB bandwidth. The inverse normalized quality factor Q_{ni} is defined as $Q_{ni} = Q_{ui}/Q_{ri}$, where Q_{ui} and Q_{ri} are the quality factors corresponding to the i th resonant point when the sample is unloaded and loaded. As shown in Fig. 5, $f_{u1} = 2.473 \text{ GHz}$, $f_{u2} = 2.286 \text{ GHz}$, $Q_{u1} = 191.705$, $Q_{u2} = 134.471$.

The response of the sensor when a sample is loaded on the permeability sensing area is depicted in Fig. 6(a). It is discovered that the resonant frequency and quality factor of the first resonant point change very little when ϵ_r' and $\tan \delta_e$ vary. They do not change noticeably until μ_r' and $\tan \delta_m$ are changed ($\mu_r' = 1.2$, $\tan \delta_m = 0.2$). No matter how the permittivity of the sample varies, the response of the first resonant point will change only when the permeability changes independently. Thus, the first resonance point can be used to compute the magnetic permeability of the SUT. When a sample is loaded on

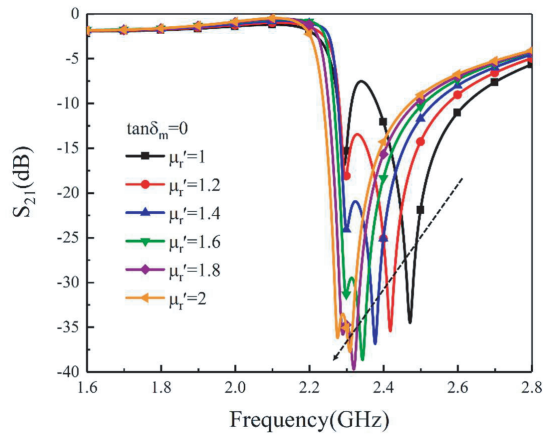


FIGURE 7. Sensor response for different μ_r' ($\tan \delta_m = 0$) when the SUTs are placed on the sensing areas.

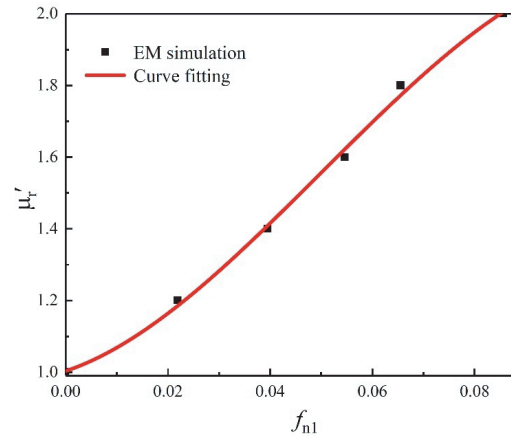


FIGURE 8. Real part of the permeability (μ_r') of the SUT versus the normalized resonant frequency shift (f_{n1}).

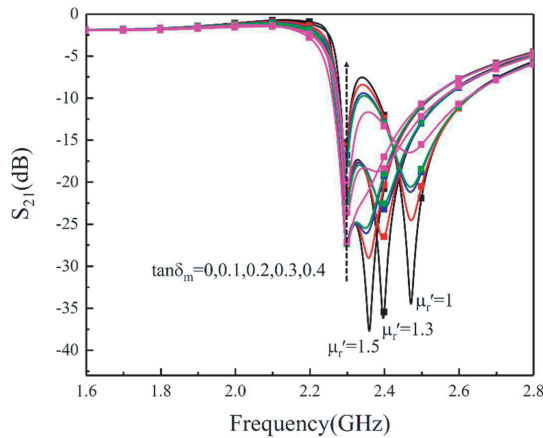


FIGURE 9. Sensor response for different $\tan \delta_m$ when SUTs are placed on the sensing area.

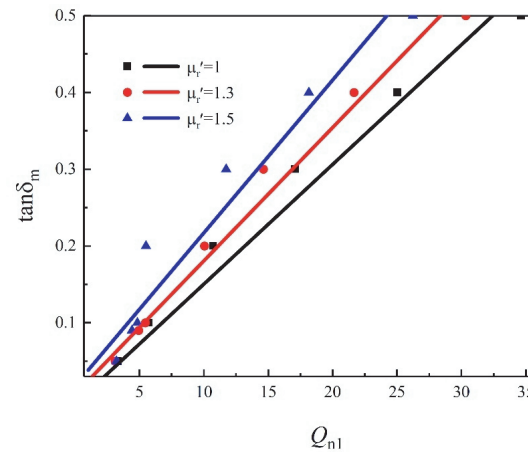


FIGURE 10. The magnetic loss tangent against the inverse normalized quality factor for different value of $\mu_r' = 1, 1.3, 1.5$.

the permittivity sensing area, the sensor response is shown in Fig. 6(b). It is found that when μ_r' and $\tan \delta_m$ change, the resonant frequency and quality factor of the second resonant point scarcely alter. Only when ϵ_r' and $\tan \delta_m$ changes ($\epsilon_r' = 10$, $\tan \delta_e = 0.1$), they change significantly. The permeability has no effect on the change in the second resonant point, which is entirely caused by variations in the permittivity. Therefore, the second resonant point can be used to measure the dielectric permittivity of SUT. It can be concluded that the electromagnetic parameters of the sample can be characterized independently by placing the SUT in different sensing areas of the resonator and detecting the resonant frequency and quality factor of its corresponding resonant point.

When the magneto-dielectric samples are positioned on the permeability and permittivity sensing area simultaneously, C_i and L_i increase, making the two resonant point shift to the low frequency. Fig. 7 further indicates that with μ_r' increasing from 1 to 2, the first resonant point shifts from 2.468 GHz to 2.306 GHz. The μ_r' increase has no impact on the second resonant frequency point, which continues to be at about 2.286 GHz. The cubic fitting relationship between μ_r' and f_{n1}

is obtained by extracting the results in Fig. 7 and is displayed in Fig. 8. The resulting mathematical model can be expressed as follows.

$$\mu_r' = 1.0045 + 4.6809f_{n1} + 186.5503f_{n1}^2 - 1221.3443f_{n1}^3 \quad (5)$$

Figure 9 illustrates that, for a fixed μ_r' , the resonant frequency remains almost unchanged with the increase of $\tan \delta_m$, but the amplitude of S_{21} and quality factor attenuate to varying degrees. To more clearly show the influence of the magnetic loss tangent on the sensor, Fig. 10 shows $\tan \delta_m$ as a function of the reverse normalized quality factor Q_{n1} at different μ_r' values. In Fig. 10, the quality factor dramatically declines when the magnetic loss tangent increases from 0 to 0.5, causing the Q_{n1} to rise from 24 to 32. The polynomial fitting tool is used to explicitly describe $\tan \delta_m$ as a function of μ_r' and Q_{n1} , creating the following numerical model.

$$\tan \delta_m = (147.8 - 3.684Q_{n1} - 2226.8\mu_r' + 0.348Q_{n1}^2 + 18.83\mu_r'Q_{n1} + 74.73\mu_r'^2) \times 10^{-3} \quad (6)$$

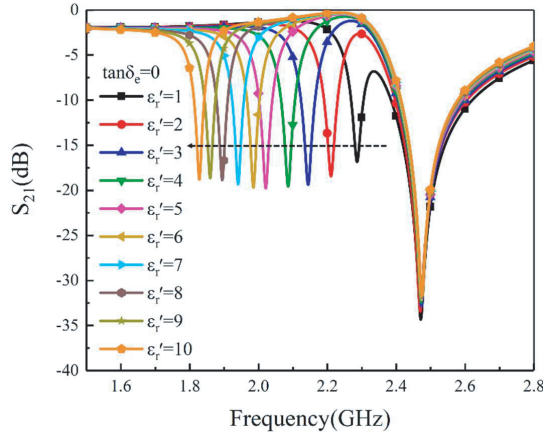


FIGURE 11. Sensor response for different ϵ_r' ($\tan \delta_e = 0$) when the SUTs are placed on the sensing areas.

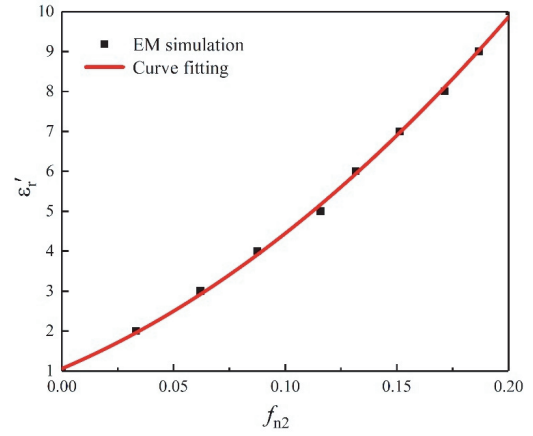


FIGURE 12. Real part of the permittivity (ϵ_r') of the SUT versus the normalized resonant frequency shift (f_{n2}).

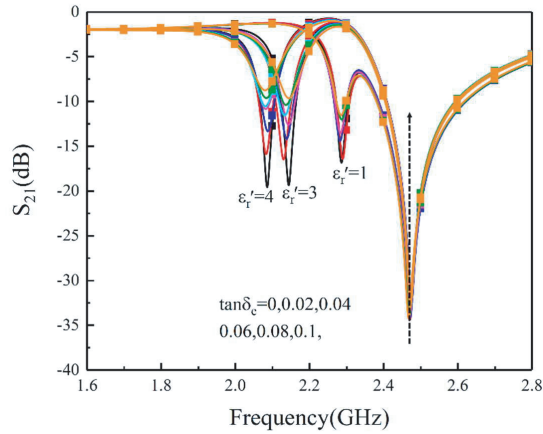


FIGURE 13. Sensor response for different $\tan \delta_e$ when SUTs are placed on the sensing area.

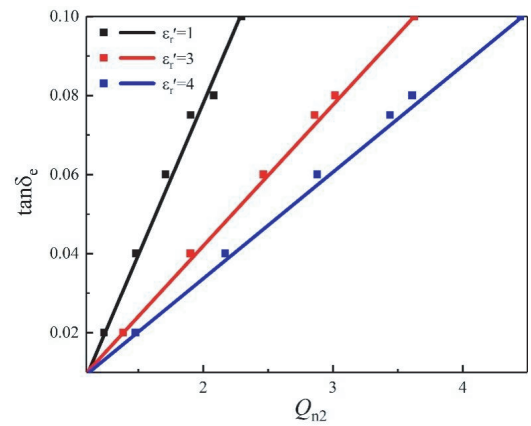


FIGURE 14. The electric loss tangent against the inverse normalized quality factor for different value of $\epsilon_r' = 1, 3, 4$.

As shown in Fig. 11, when ϵ_r' is increased from 1 to 10, the second resonant frequency point gradually moves to the low frequency, and the frequency changes from 2.291 GHz to 1.825 GHz, while the first resonant frequency is always kept around 2.473 GHz. We can infer that the second resonant frequency point is merely a function of ϵ_r' . Fig. 12 illustrates the cubic fitting relationship between ϵ_r' and f_{n2} , and the function of them is given below.

$$\epsilon_r' = 0.9101 + 33.7684f_{n2} - 31.9685f_{n2}^2 + 412.0382f_{n2}^3 \quad (7)$$

Additionally, the effect of the electric loss tangent of the SUT on the sensor response is investigated. When ϵ_r' is a fixed value, the sensor response caused by the $\tan \delta_e$ change is shown in Fig. 13. With $\tan \delta_e$ gradually increasing from 0 to 0.1, the quality factor of the second resonant point falls to variable degrees. Fig. 14 shows that $\tan \delta_e$ is a function of the reverse normalized quality factor Q_{n2} under different ϵ_r' values, which can be expressed as the following binary function.

$$\begin{aligned} \tan \delta_e = & (-10.45 + 12.56Q_{n2} + 1.664\epsilon_r' - 0.838Q_{n2}^2 \\ & - 2.93\epsilon_r'Q_{n2} + 0.0679\epsilon_r'^2 + 0.1663\epsilon_r'^2Q_{n2} \\ & + 0.1646\epsilon_r'Q_{n2}^2 + 0.0089Q_{n2}^3) \times 10^{-2} \quad (8) \end{aligned}$$

The full characterization process of material properties of magneto-dielectric samples is summarized here.

- 1) Measure the i th resonant frequency f_{ui} and its corresponding quality factor Q_{ui} when the sensor is unloaded.
- 2) The SUTs of different sizes are accurately placed on the permittivity sensing area and permeability sensing area simultaneously.
 - a) The real part of the permeability μ_r' is determined from the first resonant frequency f_{r1} using (5). The imaginary part of the permeability $\tan \delta_m$ is obtained from the quality factor Q_{r1} and μ_r' using (6).
 - b) The real part of the permittivity ϵ_r' is determined from the second resonant frequency f_{r2} using (7). The imaginary part of the permittivity $\tan \delta_e$ is obtained from the quality factor Q_{r2} , and ϵ_r' using (8).

4. EXPERIMENTAL ANALYSIS

To verify the sensing performance, a standard PCB manufacturing process was used to create the experimental prototype of the CSSR-derived microstrip sensor. The proposed sensor was

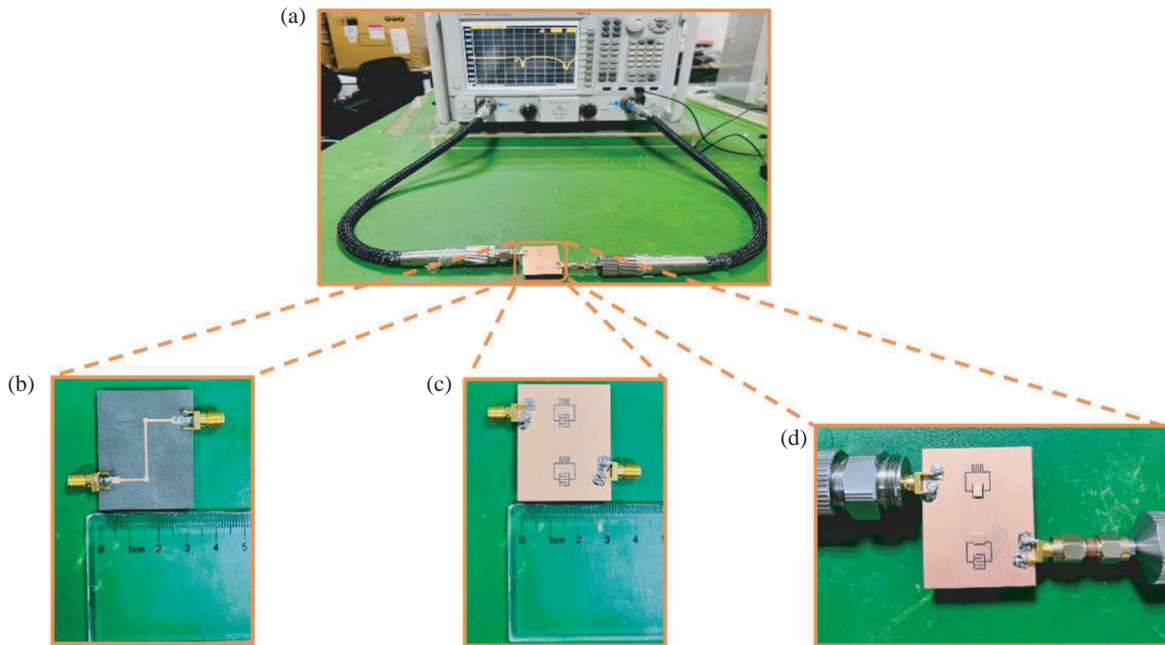


FIGURE 15. Fabricated prototype of the proposed sensor, (a) experimental setup, (b) top view of the sensor, (c) bottom view of the sensor, (d) material measurement area.

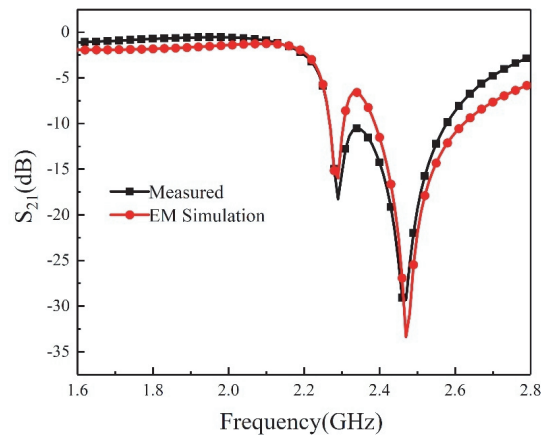


FIGURE 16. Comparison between the simulated and measured S_{21} of the unloaded sensor.

fabricated as shown in Fig. 15. The S_{21} measurements were performed at room temperature with an Agilent vector network analyzer N5242A, with the range of 1.6 GHz to 2.8 GHz. Four standard plates, Rogers RO4350, FR4, Fe_3O_4 -PDMS (30%), Fe_3O_4 -PDMS (50%), were prepared. The samples placed on the permeability sensing region and permittivity sensing area are cut to $2.6 \text{ mm} \times 3.4 \text{ mm} \times 0.5 \text{ mm}$ and $2.6 \text{ mm} \times 3.6 \text{ mm} \times 0.5 \text{ mm}$, respectively. They were precisely positioned and measured according to the position in Fig. 1.

Using two SMA connectors to excite the microstrip line, the sensor shows two unloaded resonant frequencies of 2.473 GHz and 2.286 GHz, as shown in Fig. 16. The measured results are in good agreement with the simulation ones. Different samples were placed on the corresponding sensing area at the same time. For the evaluation of repeatability and reliability, the measurement results of each sample were repeated five times at 25°C

room temperature, and the average value of the measurement results is taken. By measuring the resonant frequency f_{ri} and quality factor Q_{ri} from each sample and following the characterization procedure given in Section 3, the permeability and permittivity of the sample can be obtained simultaneously. The values of the ϵ'_r , $\tan \delta_e$, and μ'_r , $\tan \delta_m$ are shown in Table 2. It is found that the measured values are in good agreement with the nominal value given in [19, 20], indicating that the sensor can accurately measure the permittivity and permeability at the same time.

Sensitivity is also a crucial factor in determining how well a sensor performs. The sensitivities in measuring μ'_r ($\epsilon'_r = 1$, $\tan \delta_e = 0$) and ϵ'_r ($\mu'_r = 1$, $\tan \delta_m = 0$) of the sample are defined as $S_{fm} = f_{n1}/(\mu'_r - 1)$ and $S_{fe} = f_{n2}/(\epsilon'_r - 1)$ when the SUT is loaded on permeability or permittivity sensing region. Table 3 shows some parameter comparisons with litera-

TABLE 2. Measured complex permittivity and permeability for SUTs.

SUT	ϵ'_r		$\tan \delta_e$		μ'_r		$\tan \delta_m$	
	This Work	Reference	This Work	Reference	This Work	Reference	This Work	Reference
FR4 [19]	4.42	4.4	0.023	0.02	1	1	0	0
Rogers4350 [19]	3.67	3.66	0.003	0.004	1	1	0	0
Fe ₃ O ₄ (30%) [20]	2.77	2.81	0.080	0.075	1.26	1.25	0.048	0.05
Fe ₃ O ₄ (50%) [20]	2.58	2.7	0.133	0.120	1.49	1.49	0.099	0.09

TABLE 3. Comparison to previous reported sensors.

	[14]	[21]	[22]	[23]	This Work
f_u (GHz)	2.47	2.31/2.74	2.51	2.680/2.694	2.473/2.286
Q_u	145	66/91	~ 17	~ 161	192/134
$S_{fm} (\times 10^{-2}) (\mu'_r = 2)$	6.07	3.85	~	0.96	7.24
$S_{fe} (\times 10^{-2}) (\epsilon'_r = 4)$	2.83	2.19	5.84	0.58	3.06
Number of measured parameters	4	2	2	4	4
Number of tests	2	1	1	2	1

tures [14, 21–23]. The findings demonstrate that the sensor can acquire μ'_r , ϵ'_r , $\tan \delta_m$, and $\tan \delta_e$ in a single test. Compared with earlier sensors, it has more obvious advantages in obtaining higher quality factor and sensitivity.

5. CONCLUSION

In this work, a dual CSRR-derived microstrip sensor is designed, manufactured, and tested. By observing changes in resonant frequency and quality factor of the sensor, the complex permittivity and permeability of magneto-dielectric materials are measured. The meandered conductive ring and interdigital capacitor are etched at the bottom on a metal ground plate, which enhances detection sensitivity by concentrating the distribution of the magnetic and electric fields and raising S_{fm} and S_{fe} to 7.24 and 3.06. Additionally, by loading the dual CSRRs structure, it is possible to fully characterize both the dielectric and magnetic properties of the SUT in a single run, resulting in a quick and affordable measurement.

ACKNOWLEDGEMENT

This work was supported by the Chongqing Natural Science Foundation General Program (No. CSTB2022NSCQ-MSX0960), the Science and Technology Research Program of Chongqing Municipal Education Commission (No. KJQN201900622).

REFERENCES

- [1] Hofmann, M., G. Fischer, R. Weigel, and D. Kissinger, "Microwave-based noninvasive concentration measurements for biomedical applications," *IEEE Transactions on Microwave Theory and Techniques*, Vol. 61, No. 5, 2195–2204, 2013.
- [2] Raveendran, A., M. T. Sebastian, and S. Raman, "Applications of microwave materials: A review," *Journal of Electronic Materials*, Vol. 48, 2601–2634, 2019.
- [3] Mirzavand, R., M. M. Honari, and P. Mousavi, "High-resolution balanced microwave material sensor with extended dielectric range," *IEEE Transactions on Industrial Electronics*, Vol. 64, No. 2, 1552–1560, 2016.
- [4] M'Pemba, J., G. F. Bouesse, and F. M. Mbango, "Probes in transmission with material variable thicknesses to extract the material complex relative permittivity in 1.7–3 GHz," *Measurement: Sensors*, Vol. 20–21, 100369, Apr. 2022.
- [5] Guo, Y., Z. Chen, Y. Li, G. Zhao, B. Liang, and X. Yao, "Free-space measurement of dielectric and magnetic properties by double planar sample method in Y-band," *IEEE Transactions on Terahertz Science and Technology*, Vol. 12, No. 2, 182–192, 2021.
- [6] Bagci, F., M. S. Gulsu, and B. Akaoglu, "Dual-band measurement of complex permittivity in a microwave waveguide with a flexible, thin and sensitive metamaterial-based sensor," *Sensors and Actuators A: Physical*, Vol. 338, 113480, 2022.
- [7] Guo, W., H. Xo, W. Liang, and Q. Gao, "Quantitative study of near-field microwave microscopy: Application to metrology of dielectrics at nanoscale," in *2021 Cross Strait Radio Science and Wireless Technology Conference (CSRSWTC)*, 55–57, 2021.
- [8] Chakraborty, S. P., S. K. Simon, C. Bindu, J. Andrews, and V. P. Joseph, "Complex permittivity measurement using metamaterial split ring resonators," *Journal of Applied Physics*, Vol. 121, No. 5, 054101, 2017.
- [9] Schueler, M., C. Mandel, M. Puentes, and R. Jakoby, "Metamaterial inspired microwave sensors," *IEEE Microwave Magazine*, Vol. 13, No. 2, 57–68, 2012.
- [10] Ebrahimi, A., J. Scott, and K. Ghorbani, "Differential sensors using microstrip lines loaded with two split-ring resonators," *IEEE Sensors Journal*, Vol. 18, No. 14, 5786–5793, 2018.
- [11] Boybay, M. S., "Electrically small resonator design for characterization of magnetodielectric materials," in *2021 8th International Conference on Electrical and Electronics Engineering (ICEEE)*, 197–201, 2021.

- [12] Fan, L.-C., W.-S. Zhao, H.-Y. Gan, L. He, Q. Liu, L. Dong, and G. Wang, "A high-Q active substrate integrated waveguide based sensor for fully characterizing magneto-dielectric (MD) materials," *Sensors and Actuators A: Physical*, Vol. 301, 111778, 2020.
- [13] Gan, H.-Y., W.-S. Zhao, L. He, Y. Yu, K. Xu, F. Wen, L. Dong, and G. Wang, "A CSRR-loaded planar sensor for simultaneously measuring permittivity and permeability," *IEEE Microwave and Wireless Components Letters*, Vol. 30, No. 2, 219–221, 2019.
- [14] Saadat-Safa, M., V. Nayyeri, M. Khanjarian, M. Soleimani, and O. M. Ramahi, "A CSRR-based sensor for full characterization of magneto-dielectric materials," *IEEE Transactions on Microwave Theory and Techniques*, Vol. 67, No. 2, 806–814, 2019.
- [15] Alotaibi, S. A., Y. Cui, and M. M. Tentzeris, "CSRR based sensors for relative permittivity measurement with improved and uniform sensitivity throughout [0.9–10.9] GHz band," *IEEE Sensors Journal*, Vol. 20, No. 9, 4667–4678, 2019.
- [16] Zhao, W.-S., H.-Y. Gan, L. He, Q. Liu, D.-W. Wang, K. Xu, S. Chen, L. Dong, and G. Wang, "Microwave planar sensors for fully characterizing magneto-dielectric materials," *IEEE Access*, Vol. 8, 41 985–41 999, 2020.
- [17] Aznar, F., M. Gil, J. Bonache, L. Jelinek, J. D. Baena, R. Marques, and F. Martin, "Characterization of miniaturized metamaterial resonators coupled to planar transmission lines through parameter extraction," *J. Appl. Phys.*, Vol. 104, No. 11, 114501, 2008.
- [18] Gama, A. M. and M. C. Rezende, "Complex permeability and permittivity variation of carbonyl iron rubber in the frequency range of 2 to 18 GHz," *Journal of Aerospace Technology and Management*, Vol. 2, 59–62, 2010.
- [19] Alahnomi, R. A., Z. Zakaria, E. Ruslan, S. R. A. Rashid, and A. A. M. Bahar, "High-Q sensor based on symmetrical split ring resonator with spurlines for solids material detection," *IEEE Sensors Journal*, Vol. 17, No. 9, 2766–2775, 2017.
- [20] Castro, J., C. Morales, T. Weller, and J. W. Srikanth, "Synthesis and characterization of low-loss Fe₃O₄-PDMS magneto-dielectric polymer nanocomposit," in *15th IEEE Annual Conference on Wireless and Microwave Technology (WAMICON)*, 1–5, Tampa, FL, USA, 2014.
- [21] K. T., M. S., M. A. H. Ansari, A. K. Jha, and M. J. Akhtar, "Design of SRR-based microwave sensor for characterization of magnetodielectric substrates," *IEEE Microwave and Wireless Components Letters*, Vol. 27, No. 5, 524–526, 2017.
- [22] Wang, C., L. Ali, F.-Y. Meng, K. K. Adhikari, Z. L. Zhou, Y. C. Wei, D. Q. Zou, and H. Yu, "High-accuracy complex permittivity characterization of solid materials using parallel interdigital capacitor-based planar microwave sensor," *IEEE Sensors Journal*, Vol. 21, No. 5, 6083–6093, 2020.
- [23] Xiang, Y., J. Huang, L. Fu, Y. Chen, W. Gu, and Y. Wu, "A folded substrate integrated waveguide re-entrant cavity for full characterization of magneto-dielectric powder materials," *IEEE Sensors Journal*, Vol. 21, No. 9, 10 657–10 666, 2021.